

Article

Deep NIR-I Emissive Iridium(III) Complex Bearing D-A Ligand: Synthesis, Photophysical Properties and DFT/TDDFT Calculation

Jia-Yang Jiang ^{1,*}, Zi-Han Xu ^{1,†}, Tang Li ^{1,*}, Da-Hua Cai ¹, Hui Zhou ¹ and Ze-Jing Chen ^{2,*}

¹ Engineering Technology Training Center, Nanjing Vocational University of Industry Technology, 1 Yangshan North Road, Nanjing 210023, China; 2019301035@niit.edu.cn (Z.-H.X.); 1989100095@niit.edu.cn (D.-H.C.); 1990100107@niit.edu.cn (H.Z.)

² Jiangxi Key Laboratory for Nanobiomaterials, Institute of Advanced Materials (IAM), East China Jiaotong University (ECJTU), 808 Shuanggang East Main Street, Nanchang 330013, China

* Correspondence: 2019101032@niit.edu.cn (J.-Y.J.); 2019101009@niit.edu.cn (T.L.); iamzjchen@ecjtu.edu.cn (Z.-J.C.)

† These two authors contributed equally to this work.

Abstract: Near-infrared (NIR) phosphorescent iridium(III) complexes have been demonstrated to possess photophysical properties superior to those of traditional NIR dyes. However, the NIR emission wavelength is restricted in the range of 700–800 nm. For realizing deeper NIR emission, a novel type of iridium(III) complex was designed and synthesized in this work. The main ligand of the iridium(III) complex was constructed using a donor-acceptor structure containing benzothiophene as the donor and quinoxaline as the acceptor. The β -diketone derivative was chosen as the auxiliary ligand owing to its symmetrical structure and p-donating character. The complex exhibits deep NIR-I phosphorescence (764 nm in CH₂Cl₂, 811 nm in aqueous solution) and broad full width at half maximum (108 nm in CH₂Cl₂, 154 nm in aqueous solution). Theoretical calculations based on the density function and time-dependent density function were carried out to support the experimental data. Moreover, in vitro biological performance of the complex was determined as well. This work supports the possibility that via a systematic transformation between the D and A units, the photophysical performance of NIR emissive iridium(III) complexes can be greatly improved.

Keywords: iridium(III) complex; near-infrared emission; donor-acceptor structure; phosphorescence; lifetime



Citation: Jiang, J.-Y.; Xu, Z.-H.; Li, T.; Cai, D.-H.; Zhou, H.; Chen, Z.-J. Deep NIR-I Emissive Iridium(III) Complex Bearing D-A Ligand: Synthesis, Photophysical Properties and DFT/TDDFT Calculation. *Crystals* **2021**, *11*, 1038. <https://doi.org/10.3390/cryst11091038>

Academic Editor:
Jesús Sanmartín-Matalobos

Received: 6 August 2021

Accepted: 27 August 2021

Published: 29 August 2021

Publisher's Note: MDPI stays neutral with regard to jurisdictional claims in published maps and institutional affiliations.



Copyright: © 2021 by the authors. Licensee MDPI, Basel, Switzerland. This article is an open access article distributed under the terms and conditions of the Creative Commons Attribution (CC BY) license (<https://creativecommons.org/licenses/by/4.0/>).

1. Introduction

Optical molecular imaging technology is an extraordinary tool that can provide non-invasive, high-accuracy and high-resolution optical information in biomedical areas [1–4]. In order to stimulate the progress of this technology, the most important point is to promote innovations of higher-performance molecular probes [5–12]. Recently, many studies have demonstrated that regulating the probe emission wavelength to the near-infrared area is the most efficient of all performance-improving strategies [13–18]. Compared to visible light, near-infrared (NIR) light has many advantages such as less photon scattering, deeper penetration and lower tissue absorption [19–23]. Thus, the optical performance of NIR emissive probes, including signal-to-noise ratio, spatial resolution and feature contrast, can be greatly boosted in the imaging process [24–26].

Thanks to various structural engineering and functional group grafting methods, the outstanding optical properties of NIR organic molecules can now be easily realized. For example, phthalocyanine [27–29] and boron dipyrromethene dyes [30–32] can easily exhibit NIR emissions between 800 and 1000 nm and have been well investigated for in vivo applications. Methylene blue [33–35] and indocyanine green [36–39], approved by the government, have been widely used in clinical applications. However, owing to

their high chemical reactivity, most of these organic dyes can easily oxidize into molecular fragments, resulting in the loss or blue shift of luminescence. Moreover, the highly reactive excited states of NIR dyes can capture a hydrogen atom from any available source, leading to photobleaching under long-term exposure to a light source [40,41]. Moreover, the luminescence lifetime of conventional NIR molecules is limited to the range of hundreds of picoseconds to tens of nanoseconds, which cannot be distinguished from the short-lived NIR autofluorescence contributed by chlorophyll and melanin in tissues [42,43].

Compared to the traditional optical dyes mentioned above, NIR phosphorescent iridium(III) complexes have been demonstrated to possess certain superior advantages, such as high stability against photobleaching, excellent thermal stability, rich electronic characteristics, as well as long-lived phosphorescence that can be easily distinguished from autofluorescence in vivo [44–47]. Luminescent probes based on NIR iridium(III) complexes have shown reliable optical performance in biological areas. However, the NIR emission wavelength of reported iridium(III) complexes is restricted in the range of 700–800 nm, which limits their further application. Hence, exploiting deeper NIR-emission iridium(III) probes will have an important role in the development of optical imaging technology.

In this work, we reported a novel type of iridium(III) complex with deep NIR-I phosphorescence (Figure 1a). Given that donor-acceptor (D-A) type cyclometalating ligands have narrow energy gaps, which can effectively lower the triplet state (T_1) energy [48–50], a large conjugated plane containing benzothiophene as the donor and quinoxaline as the acceptor was chosen as the main ligand of the iridium(III) complex. Additionally, because symmetrical auxiliary ligands can reduce the lowest unoccupied molecular orbital (LUMO) energy of the iridium(III) complex, β -diketone derivative was selected as the auxiliary ligand [48,50]. The photophysical properties of this complex are presented in the main part of this article. Density functional theory (DFT) and time-dependent density functional theory (TDDFT) calculations were performed to thoroughly elucidate the structure-function relationship of the complex. Moreover, in vitro biological performance was determined for further applications.

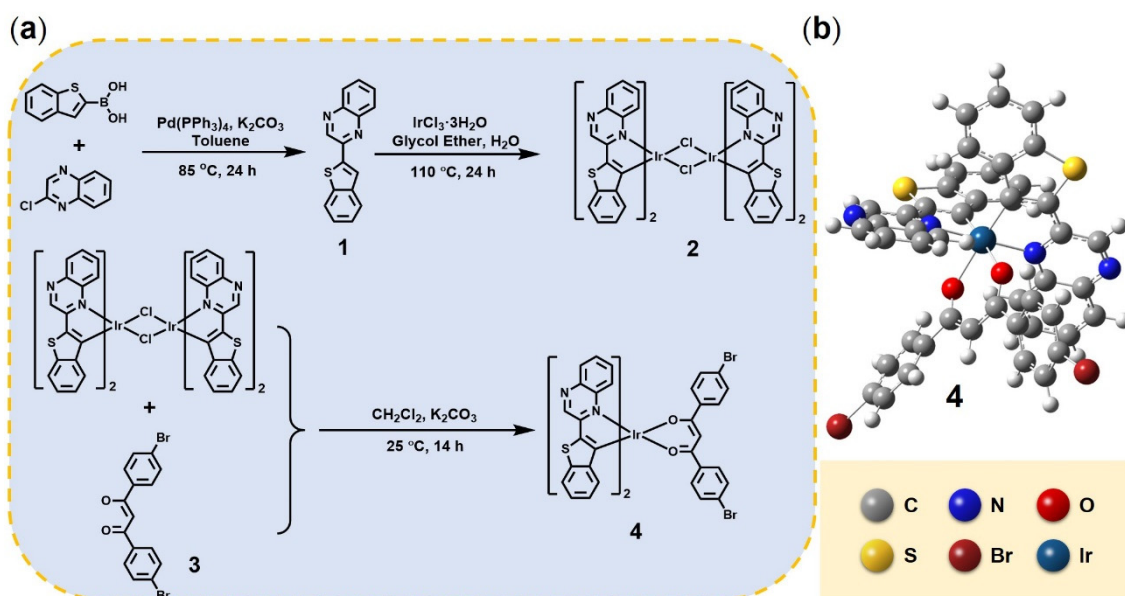


Figure 1. (a) Synthesis scheme of iridium(III) complex. The main ligand was prepared via Suzuki coupling reaction. Complex 4 was synthesized according to the typical two-step method for neutral iridium(III) complex (the cyclometalated iridium(III)-chlorobridged dimers were prepared by refluxing iridium trichloride with the main ligand, which was treated with the auxiliary ligand to obtain the final product). (b) The ground state geometric structure of complex 4 based on the B3LYP/LANL2DZ method.

2. Materials and Methods

Materials: Benzothiophen-2-ylboronic acid, 2-chloroquinoxaline, 1,3-bis(4-bromophenyl)-3-oxidanelylpropanal, tetrakis(triphenylphosphine)palladium, iridium(III) chloride hydrate, potassium hexafluorophosphate and all of the solvents were bought from Sigma-Aldrich® (Shanghai, China). All of the reagents were used without further purification unless otherwise stated. The aqueous solutions used throughout the experiment were prepared with deionized water. The supplier of cell culture flasks, culture dishes and 96-well cell culture plates was Thermo Fisher. The HeLa cell lines were purchased from KeyGEN BioTECH (Nanjing, Jiangsu, China). Dulbecco's modified eagle medium (DMEM), trypsin and fetal bovine serum (FBS) were supplied by Gibco (Nanjing, Jiangsu, China).

Instrumentation: NMR spectra were utilized to verify the compound structure, and a Bruker Ultrashield 400 Plus (Bruker, Beijing, China) instrument was employed for the measurements. To further demonstrate the validity and rationality of the complex structure, a Bruker autoflex matrix-assisted laser desorption ionization time-of-flight (MALDI-TOF) mass spectrometer was employed to record the data. The absorption measurements were conducted with a Shimadzu UV-3600 spectrophotometer (Shimadzu, Shanghai, China). The emission of the complex was recorded with an Edinburgh FL 920 spectrophotometer. Absolute quantum yields of the complex were determined in N₂ atmosphere by using an integrating sphere. An Olympus LFS-920 spectrometer (Olympus, Beijing, China) was used to assist in the study of luminescence lifetime.

2.1. Synthesis

2.1.1. Synthesis of Ligand 1

A flask contained 2-chloroquinoxaline (0.92 g, 5.60 mmol) and 1-Benzothiophen-2-ylboronic acid (1.00 g, 5.62 mmol) was prepared in advance. Then, degassed toluene (20 mL), ethanol (10 mL) and 2 M K₂CO₃ aqueous solution (8 mL) was injected. The mixture was vigorously stirred under N₂ atmosphere at 85 °C for 20 h. After shutting down the heating equipment, the mixture was extracted with water and dichloromethane. The organic layer was treated by reduced pressure distillation and the raw product was purified by column chromatogram using the mixture of dichloromethane and petroleum ether (3: 2, *v:v*) to obtain the white powder. Yield: 81%. ¹H NMR (400 MHz, CDCl₃): δ (ppm): δ 9.37 (s, 1H), 8.14–8.08 (m, 2H), 8.11 (s, 1H), 7.92–7.87 (m, 2H), 7.80–7.71 (m, 2H), 7.42–7.40 (m, 2H).

2.1.2. Synthesis of Iridium(III) Complex 4

Compound 2: IrCl₃·3H₂O (1.5 g, 4.25 mmol) and ligand 1 (2.45 g, 9.35 mmol) were dissolved with 2-ethoxyethanol and water (40 mL, 3:1, *v:v*). Then, the mixture was heated at 110 °C under N₂ atmosphere for 1 day. After shutting down the heating equipment, the dark brown precipitate was acquired by filtering and washed with a solution of water and ethanol.

Complex 4: After a mixture of compound 2 (1.20 g, 0.67 mmol), 1,3-bis(4-bromophenyl) propane-1,3-dione (0.56 g, 1.47 mmol) and excess ground K₂CO₃ was added into the flask, 60 mL degassed CH₂Cl₂ was injected. The flask was set at room temperature under nitrogen for 14 h accompanied with vigorous stirring. Then, the mixture was extracted with water and dichloromethane. The organic layer was treated by reduced pressure distillation and the raw product was purified by column chromatogram using the mixture of petroleum ether, ethyl acetate and dichloromethane (1:2:2, *v:v:v*). Yield: 13%. ¹H NMR (400 MHz, CDCl₃) δ (ppm): δ 9.26 (s, 2H), 8.01 (d, *J* = 8.3 Hz, 2H), 7.90–7.79 (m, 4H), 7.44–7.37 (m, 8H), 7.28–7.24 (m, 2H), 7.13 (t, *J* = 7.5 Hz, 2H), 7.02–6.98 (m, 2H), 6.65 (t, *J* = 7.6 Hz, 2H), 6.34–6.31 (m, 2H), 5.30 (s, 1H). MALDI-TOF-MS *m/z*: 1095.78.

2.2. Computational Details

Density functional theory (DFT) calculations in conjunction with different basis set calculations were performed with the assistance of the Gaussian 09 package. The full

geometry optimizations of iridium(III) complex both in the ground and excited state were optimized using the Becke's three-parameter Lee–Yang–Parr (B3LYP) hybrid density functional method. The LANL2DZ basis set was employed for iridium(III) atoms, and the 6–31G (d, p) basis set was employed for other non-metal atoms. The highest occupied molecular orbital (HOMO) and LUMO energy levels were calculated via DFT as well. After optimization of the ground and excited states, time-dependent density functional theory (TDDFT) method was applied to predict UV–visible spectra, singlet and triplet energy levels.

2.3. Cell Viability Assessment

Before cell viability assessment, Hela cancer cells were cultured in DMEM and supplemented with 10% (*v:v*) FBS at 37 °C. The cells were maintained under the atmosphere of 5% CO₂. The methyl thiazolyl tetrazolium (MTT) test was conducted to assess the *in vivo* cytotoxicity of complex 4 toward Hela cells. First, cells growing in exponential period were suspended by trypsin and cultured in a 96-well cell plate at proper concentration. Then, the solution of complex 4 was dropped into the cell plate with the concentrations of 0, 5, 10, 20 and 40 µM. The following day, cells were cultured with MTT solution (5 mg/mL in PBS solution) in each well. About 4 h later, all of the culture solution in the cell plate was removed and DMSO (dimethylsulfoxide) was added with the volume of 150 µL. Then, the optical density (OD value, monitored at 570 nm) was measured by a microplate reader after shaking the cell plate for 10 min. The collected data was analyzed using OriginPro 8.5 software.

3. Results and Discussion

3.1. Structural Characterization

The chemical structures and synthesis routes of compounds investigated in this work are displayed in Figure 1. The main ligand (compound 1) was prepared in high yield (81%) according to the classic Suzuki C–C coupling reaction. The necessary recrystallization steps of compound 1 should be conducted to improve the yields of subsequent coordination reaction. After the coordination of compound 1 to the cyclometalated iridium(III)-chlorobridged dimers (compound 2), the crude target product was acquired in a relatively low yield. This was because the main ligand bearing two nitrogen atoms formed a different, undesired coordinate structure with the iridium center. Meanwhile, the poor solubility of the auxiliary ligand limited the collision probability of the coordinate reaction as well. Compared to other NIR iridium(III) complexes, which utilize strong electron-withdrawing groups (e.g., –CF₃) and electron-withdrawing groups (e.g., –NCH₃) to regulate the energy gaps, the synthetic complexity and cost of complex 4 was more acceptable. All new compounds were characterized by ¹H NMR spectrometry and MODI-TOF (Figures S1–S3). It can be observed in ¹H NMR spectra that the chemical shift of benzene protons of ligand 1 (H-3, 9.37 ppm) moved to low field (9.26 ppm) after the final coordination reaction. This result indicates a reduced deshielding effect and the effective coordination between the iridium(III) center and ligand 1.

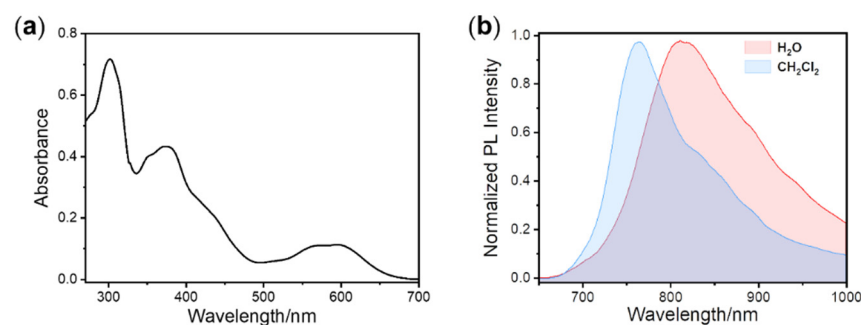
3.2. Absorption and Emission Studies

To investigate excited state properties, the UV-Vis absorption spectrum of complex 4 was studied first (Figure 2). The representative absorption data are summarized in Table 1. As depicted in Figure 2a, the strong absorption signal around 300 nm is attributed to ¹π–π* transitions in the organic conjugated ligands. The weaker absorption band between 340 and 500 nm is attributed to the spin-allowed singlet metal-to-ligand charge-transfer (¹MLCT) and ligand-to-ligand charge-transfer (¹LLCT) transitions. The lowest and structure-less absorption bands above 595 nm are attributed to the mixture of ¹MLCT and triplet metal-to-ligand charge transfer (³MLCT) transitions. The typical shape of the absorption spectrum proves that the noteworthy spin–orbit coupling between T₁ and singlet (S₁) states occurs due to the heavy-atom effect of the iridium atom [46,47].

Table 1. Photophysical data of Ir(III) complex **4**.

| Solvent | $\lambda_{\text{abs}}/\text{nm}$ | $\epsilon/10^5/\text{M}^{-1}/\text{cm}^{-1}$ | $\lambda_{\text{em}}/\text{nm}$ ^b | τ/ns ^c | Φ ^d |
|---------------------------------|----------------------------------|--|--|-------------------------------|---------------------|
| CH ₂ Cl ₂ | 302, 373, 594 | 0.66, 0.43, 0.18 | 764 | 257 | 0.016 |
| H ₂ O | 303, 377, 596 | 0.57, 0.39, 0.11 | 811 | 78 | 0.007 |

^a All data were collected in a 1 cm width quartz cell. The sample concentration was 50 μM . ^b 405 nm light was used as the excitation source. ^c Luminescence lifetime was determined in air at room temperature. ^d Absolute quantum efficiency was collected via an integrating sphere under the atmosphere of N₂ at room temperature.

**Figure 2.** (a) UV/vis absorption spectrum of complex **4**; (b) Emission spectra of complex **4** under 405 nm excitation. The concentration of complex **4** was 50 μM .

In order to further study the properties of the excited state, the emission spectra of iridium(III) complex were acquired. The PL spectra measured in CH₂Cl₂ and aqueous solution at room temperature are shown in Figure 2b, and the representative data are listed separately in Table 1. It is seen that the main phosphorescence emissions were in the range of 700–1000 nm, which are located in the deep NIR-I region. Because of the electron-donating character of its S atom and its large rigid plane skeleton, benzothiophene was selected to serve as the electron donor in the main ligand. Meanwhile, owing to the relatively high electronegativity of the two N atoms, the quinoxaline could easily withdraw the delocalized electron and act as an electron acceptor group. The combination of benzothiophene and quinoxaline could promote the charge transfer within the ligand and narrow the HOMO-LUMO gap (HLG), resulting in the deep NIR-I emission. In addition, the maximum emission peaks of the PL spectra were at 764 nm and 811 nm in solution of CH₂Cl₂ and deionized water, respectively. On account of the aggregation effect of complex **4** in aqueous solution, the molecular rigidity increased. The inhibition of intermolecular rotation and the promotion of molecule coplanarity formed a larger π -conjugated structure, resulting in a remarkable bathochromic shift of about 47 nm in the emission spectra. Moreover, the full width at half maximum (FWHM) of the PL spectra reached 108 nm and 154 nm in CH₂Cl₂ and deionized water, respectively, implying the active energy relaxation and rich excited state levels of complex **4**. Utilizing an integrating sphere, the PL quantum yields (Table 1) of the iridium(III) phosphors were measured to be 1.6% in CH₂Cl₂ and 0.7% in deionized water. This phenomenon may be interpreted as a result of the low HOMO-LUMO gap, which facilitates the nonradiative decay process, causing the high dissipation of excited state energy. The above obtained results demonstrate that by selecting the appropriate ancillary ligands, the emission wavelength of the iridium(III) complexes can be significantly regulated into the NIR area. Moreover, because of the rich electron characteristics and highly coupled energy levels of the transition metal complexes, the efficient intersystem crossing, reflected by the long-lived phosphorescence, can be easily observed. The luminescence lifetime fitting curves of complex **4** (Figure S4) were determined to be 257 ns and 79 ns in CH₂Cl₂ and deionized water, respectively, which indicates that complex **4** can be used as a promising optical probe for high accuracy luminescence lifetime imaging or detection (Table 1).

3.3. Theoretical Calculation of DFT

For a deeper understanding the photophysical properties, theoretical investigations were performed on complex **4**. First of all, the geometry of complex **4** was optimized by using B3LYP/LANL2DZ. The optimized ground-state geometries of complex **4** are displayed in Figure 1b. As shown, a slightly twisted octahedron coordination geometry was adopted by complex **4**. Owing to the d^6 electron shell of the Ir(III) ion, the classical chelating configurations of cis O-O, cis C-C, and trans N-N were calculated and found to be similar to those most reported.

As we know, the frontier molecular orbital (FMO) is a vital theoretical tool to study the optical and chemical properties of the complex. Using DFT, the FMO of complex **4** was calculated and is illustrated in Figure S5. According to the calculation data for ground state, the HOMO is mainly contributed by the d_{π} orbital of the central iridium atom and the π orbital of thiophene groups in the main ligand. In comparison, the LUMO is mainly distributed on the π^* orbital of the quinoxaline groups in the main ligand. It is worth noting that HOMO - 2, HOMO - 5, LUMO + 2 and LUMO + 5 orbits are distributed on the β -diketonate ligand, which means that the auxiliary ligand effectively participates in the excited state. Furthermore, the excited state FMO of complex **4** was also calculated. Compared to the ground state information, the structure of complex **4** in the excited state was almost unchanged (Figure S6) and the electron cloud distribution of excited state HOMO and LUMO were almost the same.

To assist in the attribution of electron transition, the absorption spectra of complex **4** were calculated through TDDFT analysis after optimization of the ground state geometry. The corresponding calculated excitation energies, oscillatory strength, and transition assignments are given in Table 2 and Figure 3a. The simulated absorption spectrum of complex **4** is shown in Figure 3b. As is seen in Table 2 and Figure 3, there are intense absorption bands of complex **4** centered at 448, 452, 476 and 578 nm. The lowest energy excitation at 578 nm was assigned to HOMO-LUMO transition with the configuration coefficient of 0.70. According to the DFT calculation above (Figure 4), this absorption band can be attributed to the mixture of MLCT and intraligand charge transfer (ILCT). The wavelength of the simulated lowest energy absorption peak was in accordance with the experimental data (594 nm). Owing to the application of Gaussian smearing, which can prevent the discontinuous change in the total calculation of energy, the intensity of the simulated lowest absorption peak appeared relatively weaker than that based on the experimental data. In order to depict the electron transition intuitively, the FMOs in the singlet state are illustrated in Figure 4a.

Table 2. TD-DFT calculation of representative excitation state and transition assignment of complex **4**.

| Spin State ^a | λ_{abs} (nm) (Calcd) | Oscillator Strength | Major Transition (s) | Character |
|-------------------------|--|------------------------|--|------------------------|
| S ₁ | 578 | 0.0149 | HOMO→LUMO (0.70) | MLCT/ILCT |
| S ₂ | 576 | 0.1006 | HOMO→LUMO + 1 (0.70) | MLCT/ILCT |
| S ₃ | 483 | 0.0050 | HOMO→LUMO + 2 (0.70) | MLCT/LLCT |
| S ₄ | 452 | 0.1137 | HOMO - 1→LUMO (0.70) | MLCT/ILCT |
| S ₅ | 450 | 0.0185 | HOMO - 5→LUMO (0.10) HOMO - 2→LUMO (0.69) | MLCT/LLCT MLCT/LLCT |
| S ₆ | 448 | 0.0470 | HOMO - 1→LUMO + 1 (0.69) | MLCT/ILCT |
| T ₁ | 832 | 0.0000 | HOMO→LUMO (0.65) HOMO - 1→LUMO + 1 (0.23) | MLCT/ILCT MLCT/LLCT |

^a The S_n and T₁ excitation states were calculated on the basis of the ground state and excited state geometry, respectively.

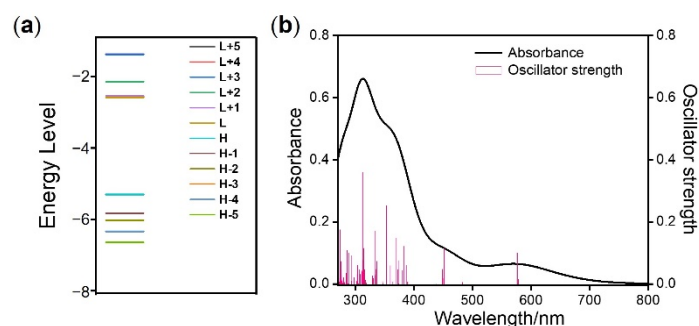


Figure 3. (a) DFT-calculated FMO energy diagram. (b) Absorption spectra for complex **4** calculated on the basis of TDDFT.

On the basis of Kasha's rule (photoluminescence results from the lowest excited state T_1) and spin-orbit coupling effect [51], all the excited energies of complex **4** would tend to arrive at the T_1 state via internal conversion or intersystem crossing. Thus, the investigation of T_1 state is the only requirement here. The calculated information for excited triplet energy levels is shown in Table 2 and Figure 4b. It was found that the excited state T_1 is contributed by the LUMO-HOMO and LUMO + 1-HOMO - 1 transition. Additionally, the configuration coefficient of the two dominating transitions was 0.65 and 0.23, respectively. Corresponding to the above analysis in Figure S7, the transition at triplet state could be described as the mixture of MLCT, ILCT and LLCT. In general, the active electron transition of complex **4** suggests that the D-A characteristic of the main ligand has a significant impact on the excited state. Moreover, the calculated absorption spectrum for complex **4** was roughly the same as the experimental one, which proved the accuracy of this calculation method.

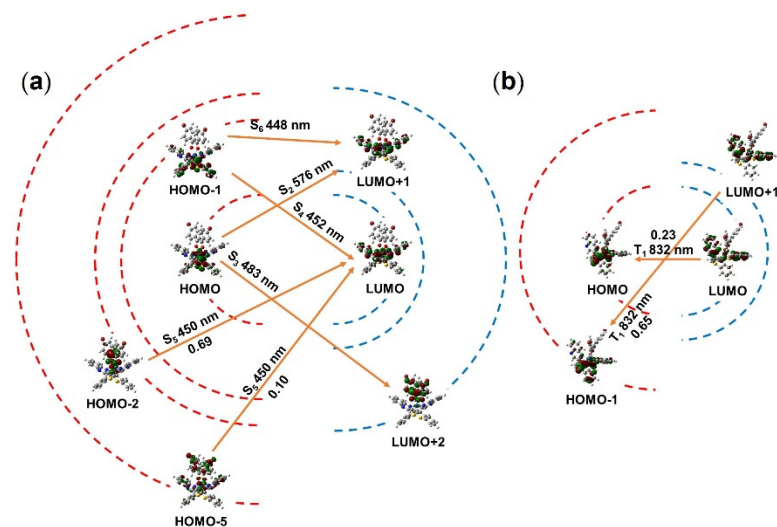


Figure 4. (a,b) Abridged general view of singlet and triplet transitions of complex **4**, respectively. The red dashed lines represent the HOMOs and the blue dashed lines represent the LUMOs (the transverse distances of the dashed lines only give a rough indication of FMO energy gaps). The orange arrows represent the transition between FMOs according to theoretical calculations.

3.4. Biological Application Performance

Chemical stability is a vital factor for evaluating the application value of optical probes. For testing the chemical stability of complex **4**, the sample dissolved in deionized water was preserved at room temperature for 1 month. As displayed in Figure 5a, little decrease was observed at the emission of 811 nm, implying the stable chemical reactivity of the ground-state complex **4**. Moreover, photobleaching resulting from the cleaving of covalent bonds under light irradiation is another important reference parameter for

imaging applications. The photostability of complex **4** in deionized water was assessed under 532 nm laser irradiation for 30 min (Figure 5b). With the increase in irradiation time, the emission intensity at 811 nm of complex **4** remained over 90% of its initial intensity. This result shows that complex **4** in the excited state is capable of resisting dissociation from interaction with photons, oxygen and other molecules, indicating better photostability than traditional small molecular dyes thanks to its unreactive excited state and steady conjugated ligand. All the data collected above indicated that complex **4** should be a promising phosphorescent probe.

To further demonstrate the biological application performance of complex **4**, a cytotoxicity assessment was conducted utilizing the 3-(4,5-dimethyl-2-thiazolyl)-2,5-diphenyltetrazolium bromide (MTT) assay. As shown in Figure 5c, after incubation with 20 μM complex **4** (a concentration much higher than conventional dosage of dyes) for 24 h, the viability of Hela cells remained above 80%. Even at the highest concentration of 40 μM , over 70% cells were alive. This result proves that complex **4** has almost no cytotoxicity *in vivo*.

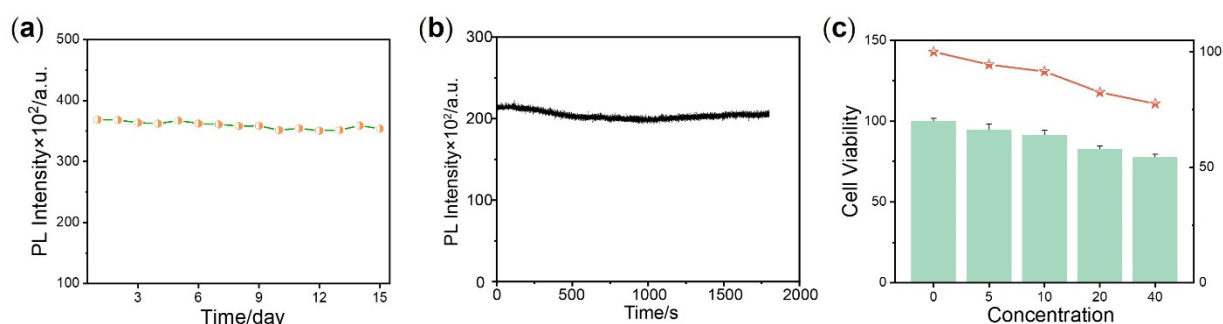


Figure 5. (a) The chemical stability test of complex **4**. The sample was preserved at room temperature for 0.5 month, and the PL intensity was measured every other day. (b) The photostability test of complex **4**. The sample was exposed under 532 nm xenon lamp and the PL intensity was measured within 30 min. Complex **4** was dissolved in CH_2Cl_2 at the concentration of 50 μM . The excitation wavelength was 532 nm, and the emission at 764 nm was collected in (a,b). (c) MMT assay of complex **4**. The green bar graphs represent the cellular viability and the orange plot shows the correlation trend between concentration and cellular viability.

4. Conclusions

In summary, a novel type of cyclometalated iridium complex **4** was designed and prepared. A donor-acceptor structure containing benzothiophene (donor) and quinoxaline (acceptor) was used as the main ligand of complex **4**. β -diketone derivative was chosen to be the auxiliary ligand. The complex exhibited a red-light absorption spectrum and a broad emission band in the deep NIR-I region. According to the DFT/TDDFT calculations, the D-A structure of the main ligand and the extended π -conjugation of the β -diketonate ligand have a prominent impact on electron density distributions of the molecular orbitals, HLG energies and absorption spectra. Moreover, *in vitro* tests of biological performance including photostability and cytotoxicity proved that complex **4** can serve as a potential clinical optical probe after further development. The next step in this work will focus on improving the water dispersibility of complex **4** and developing multifunctional probes for microenvironmental detection *in vivo*.

Supplementary Materials: The following are available online at <https://www.mdpi.com/article/10.3390/cryst11091038/s1>, Table S1: The frontier orbital energy for complex **4**, Figures S1 and S2: ¹H-NMR spectra of ligand and complex **4**, Figure S3: MALDI-TOF spectrum of complex **4**, Figure S4: Transient photoluminescence decay spectra of complex **4**, Figure S5: Isodensity plots of ground state frontier orbitals of complex **4**, Figure S6: The excited state geometry structure of complex **4**, Figure S7: Isodensity plots of excited state frontier orbitals of complex **4**.

Author Contributions: Conceptualization, J.-Y.J.; methodology, J.-Y.J. and Z.-H.X.; software, T.L.; validation, J.-Y.J. and Z.-H.X.; investigation, D.-H.C. and H.Z.; resources, J.-Y.J., T.L. and Z.-J.C.; data curation, J.-Y.J. and Z.-H.X.; writing—original draft preparation, J.-Y.J. and Z.-H.X.; writing—review and editing, J.-Y.J. and Z.-H.X. All authors have read and agreed to the published version of the manuscript.

Funding: This research was funded by the 2020 General Projects of Natural Science Research in Colleges and Universities of Jiangsu Province (20KJB150048), the Starting Research Fund of Nanjing Vocational University of Industry Technology (YK20-14-02), the National Natural Science Foundation of China (22001069), the Natural Science Foundation of Jiangxi Province (20202BAB214012), the Science and Technology Research Project of Jiangxi Provincial Department of Education (GJJ190350) and the open research fund of Key Laboratory for Organic Electronics and Information Displays.

Conflicts of Interest: The authors declare no conflict of interest.

References

1. Tang, J.; Ren, J.; Han, K.Y. Fluorescence Imaging with Tailored Light. *Nanophotonics* **2019**, *8*, 2111–2128. [[CrossRef](#)]
2. Sahl, S.J.; Hell, S.W.; Jakobs, S. Fluorescence Nanoscopy in Cell Biology. *Nat. Rev. Mol. Cell. Biol.* **2017**, *18*, 685–701. [[CrossRef](#)]
3. Yang, W.; Chen, S.-L. Time-Gated Fluorescence Imaging: Advances in technology and biological applications. *J. Innov. Opt. Health Sci.* **2020**, *13*, 2030006. [[CrossRef](#)]
4. Cheng, P.; Pu, K. Molecular Imaging and Disease Theranostics with Renal-Clearable Optical Agents. *Nat. Rev. Mater.* **2021**, 1–19. [[CrossRef](#)]
5. Klymchenko, A.S. Solvatochromic and Fluorogenic Dyes as Environment-Sensitive Probes: Design and biological applications. *Acc. Chem. Res.* **2017**, *50*, 366–375. [[CrossRef](#)] [[PubMed](#)]
6. Smith, B.R.; Gambhir, S.S. Nanomaterials for In Vivo Imaging. *Chem. Rev.* **2017**, *117*, 901–986. [[CrossRef](#)]
7. Gao, M.; Yu, F.; Lv, C.; Choo, J.; Chen, L. Fluorescent chemical probes for accurate tumor diagnosis and targeting therapy. *Chem. Soc. Rev.* **2017**, *46*, 2237–2271. [[CrossRef](#)]
8. Cheng, M.H.Y.; Mo, Y.; Zheng, G. Nano Versus Molecular: Optical Imaging Approaches to Detect and Monitor Tumor Hypoxia. *Adv. Healthc. Mater.* **2021**, *10*, 2001549. [[CrossRef](#)]
9. Wei, Y.; Liu, Y.; He, Y.; Wang, Y. Mitochondria and Lysosome-Targetable Fluorescent Probes for Hydrogen Peroxide. *J. Mater. Chem. B* **2021**, *9*, 908–920. [[CrossRef](#)]
10. Yokota, T.; Fukuda, K.; Someya, T. Recent Progress of Flexible Image Sensors for Biomedical Applications. *Adv. Mater.* **2021**, *33*, 2004416. [[CrossRef](#)] [[PubMed](#)]
11. East, A.K.; Lucero, M.Y.; Chan, J. New Directions of Activity-Based Sensing for In Vivo NIR Imaging. *Chem. Sci.* **2021**, *12*, 3393–3405. [[CrossRef](#)]
12. Zhang, Y.; Zhao, W.; Chen, Y.; Yuan, H.; Fang, H.; Yao, S.; Zhang, C.; Xu, H.; Li, N.; Liu, Z. Rational Construction of A Reversible Arylazo-Based NIR Probe for Cycling Hypoxia Imaging In Vivo. *Nat. Commun.* **2021**, *12*, 2772. [[CrossRef](#)]
13. Hong, G.; Antaris, A.L.; Dai, H. Near-Infrared Fluorophores for Biomedical Imaging. *Nat. Biomed. Eng.* **2017**, *1*, 0010. [[CrossRef](#)]
14. Li, J.; Pu, K. Development of Organic Semiconducting Materials for Deep-Tissue Optical Imaging, Phototherapy and Photoactivation. *Chem. Soc. Rev.* **2019**, *48*, 38–71. [[CrossRef](#)]
15. Yang, S.J.; Del Bonis-O'Donnell, J.T.; Beyene, A.G.; Landry, M.P. Near-Infrared Catecholamine Nanosensors for High Spatiotemporal Dopamine Imaging. *Nat. Protoc.* **2021**, *16*, 3026–3048. [[CrossRef](#)] [[PubMed](#)]
16. Cui, S.; Yin, D.; Chen, Y.; Di, Y.; Chen, H.; Ma, Y.; Achilefu, S.; Gu, Y. In Vivo Targeted Deep-Tissue Photodynamic Therapy Based on Near-Infrared Light Triggered Upconversion Nanoconstruct. *ACS Nano* **2013**, *7*, 676–688. [[CrossRef](#)] [[PubMed](#)]
17. Huang, L.; Li, Z.; Zhao, Y.; Yang, J.; Yang, Y.; Pendharkar, A.I.; Zhang, Y.; Kelmar, S.; Chen, L.; Wu, W. Enhancing Photodynamic Therapy Through Resonance Energy Transfer Constructed Near-Infrared Photosensitized Nanoparticles. *Adv. Mater.* **2017**, *29*, 1604789. [[CrossRef](#)] [[PubMed](#)]
18. Li, J.; Pu, K. Semiconducting polymer nanomaterials as near-infrared photoactivatable protherapeutics for cancer. *Acc. Chem. Res.* **2020**, *53*, 752–762. [[CrossRef](#)]
19. Huang, J.; Pu, K. Near-Infrared Fluorescent Molecular Probes for Imaging and Diagnosis of Nephro-Urological Diseases. *Chem. Sci.* **2021**, *12*, 3379–3392. [[CrossRef](#)] [[PubMed](#)]
20. Yan, C.; Zhang, Y.; Guo, Z. Recent Progress on Molecularly Near-Infrared Fluorescent Probes for Chemotherapy and Phototherapy. *Coord. Chem. Rev.* **2021**, *427*, 213556. [[CrossRef](#)]
21. Usama, S.M.; Inagaki, F.; Kobayashi, H.; Schnermann, M.J. Norcyanine-Carbamates are Versatile Near-Infrared Fluorogenic Probes. *J. Am. Chem. Soc.* **2021**, *143*, 5674–5679. [[CrossRef](#)]
22. Li, L.; Han, X.; Wang, M.; Li, C.; Jia, T.; Zhao, X. Recent Advances in the Development of Near-Infrared Organic Photothermal Agents. *Chem. Eng. J.* **2021**, 128844. [[CrossRef](#)]
23. Yuan, L.; Lin, W.; Zheng, K.; He, L.; Huang, W. Far-Red to Near Infrared Analyte-Responsive Fluorescent Probes Based on Organic Fluorophore Platforms for Fluorescence Imaging. *Chem. Soc. Rev.* **2013**, *42*, 622–661. [[CrossRef](#)]

24. Wu, D.; Chen, L.; Lee, W.; Ko, G.; Yin, J.; Yoon, J. Recent Progress in the Development of Organic Dye Based Near-Infrared Fluorescence Probes for Metal Ions. *Coord. Chem. Rev.* **2018**, *354*, 74–97. [[CrossRef](#)]
25. Guo, Z.; Park, S.; Yoon, J.; Shin, I. Recent progress in the development of near-infrared fluorescent probes for bioimaging applications. *Chem. Soc. Rev.* **2014**, *43*, 16–29. [[CrossRef](#)]
26. Swamy, P.C.A.; Sivaraman, G.; Priyanka, R.N.; Raja, S.O.; Ponnuvel, K.; Shanmugpriya, J.; Gulyani, A. Near Infrared (nir) Absorbing Dyes as Promising Photosensitizer for Photo Dynamic Therapy. *Coord. Chem. Rev.* **2020**, *411*, 213233. [[CrossRef](#)]
27. Josefsen, L.B.; Boyle, R.W. Unique Diagnostic and Therapeutic Roles of Porphyrins and Phthalocyanines in Photodynamic Therapy, Imaging and Theranostics. *Theranostics* **2012**, *2*, 916. [[CrossRef](#)] [[PubMed](#)]
28. Li, X.; Kim, C.-y.; Lee, S.; Lee, D.; Chung, H.-M.; Kim, G.; Heo, S.-H.; Kim, C.; Hong, K.-S.; Yoon, J. Nanostructured Phthalocyanine Assemblies with Protein-Driven Switchable Photoactivities for Biophotonic Imaging and Therapy. *J. Am. Chem. Soc.* **2017**, *139*, 10880–10886. [[CrossRef](#)] [[PubMed](#)]
29. Zhang, Y.; Lovell, J.F. Recent Applications of Phthalocyanines and Naphthalocyanines for Imaging and Therapy. *Wires Nanomed. Nanobiotechnol.* **2017**, *9*, e1420. [[CrossRef](#)]
30. Boens, N.; Leen, V.; Dehaen, W. Fluorescent Indicators Based on Bodipy. *Chem. Soc. Rev.* **2012**, *41*, 1130–1172. [[CrossRef](#)] [[PubMed](#)]
31. Duan, C.; Won, M.; Verwilt, P.; Xu, J.; Kim, H.S.; Zeng, L.; Kim, J.S. In Vivo Imaging of Endogenously Produced HClO in Zebrafish and Mice Using a Bright, Photostable Ratiometric Fluorescent probe. *Anal. Chem.* **2019**, *91*, 4172–4178. [[CrossRef](#)]
32. Ji, X.; Wang, N.; Zhang, J.; Xu, S.; Si, Y.; Zhao, W. Meso-Pyridinium Substituted Bodipy Dyes as Mitochondria-Targeted Probes for the Detection of Cysteine in Living Cells and In Vivo. *Dye. Pigment.* **2021**, *187*, 109089. [[CrossRef](#)]
33. Jing, X.; Zhi, Z.; Zhang, N.; Song, H.; Xu, Y.; Zhou, G.; Wang, D.; Shao, Y.; Meng, L. Multistage Tumor Microenvironment-Responsive Theranostic Nanoparticles: Toward Multimode Imaging Guided Chemo-Photodynamic Therapy. *Chem. Eng. J.* **2020**, *385*, 123893. [[CrossRef](#)]
34. Wei, H.-G.; Liu, Y.-J.; Zhao, X.-D. Methylene Blue-Based 7-Nitro-1, 2, 3-Benzoxadiazole NIR Fluorescent Probe Triggered by H₂S. *Bioorg. Med. Chem. Lett.* **2020**, *30*, 127221. [[CrossRef](#)]
35. Ma, K.; Zhao, L.; Yue, Y.; Huo, F.; Chao, J.; Yin, C. Thiol “Click” Chromene Ring Opening and Subsequent Cascade Nucleophilic Cyclization NIR Fluorescence Imaging Reveal High Levels of Thiol in Drug-Resistant Cells. *Anal. Chem.* **2020**, *92*, 15936–15942. [[CrossRef](#)]
36. Alius, C.; Tudor, C.; Badiu, C.D.; Dascalu, A.M.; Smarandache, C.G.; Sabau, A.D.; Tanasescu, C.; Balasescu, S.A.; Serban, D. Indocyanine Green-Enhanced Colorectal Surgery—Between being Superfluous and being A Game-Changer. *Diagnostics* **2020**, *10*, 742. [[CrossRef](#)]
37. Liu, C.; Cao, Y.; Cheng, Y.; Wang, D.; Xu, T.; Su, L.; Zhang, X.; Dong, H. An Open Source and Reduce Expenditure ROS Generation Strategy for Chemodynamic/Photodynamic Synergistic Therapy. *Nat. Commun.* **2020**, *11*, 1–9. [[CrossRef](#)]
38. Younis, M.R.; Wang, C.; An, R.; Wang, S.; Younis, M.A.; Li, Z.-Q.; Wang, Y.; Ihsan, A.; Ye, D.; Xia, X.-H. Low Power Single Laser Activated Synergistic Cancer Phototherapy Using Photosensitizer Functionalized Dual Plasmonic Photothermal Nanoagents. *ACS Nano* **2019**, *13*, 2544–2557. [[CrossRef](#)] [[PubMed](#)]
39. Cao, J.; Chi, J.; Xia, J.; Zhang, Y.; Han, S.; Sun, Y. Iodinated Cyanine Dyes for Fast Near-Infrared-Guided Deep Tissue Synergistic Phototherapy. *ACS Appl. Mater. Inter.* **2019**, *11*, 25720–25729. [[CrossRef](#)] [[PubMed](#)]
40. Kong, X.; Nir, E.; Hamadani, K.; Weiss, S. Photobleaching Pathways in Single-Molecule FRET Experiments. *J. Am. Chem. Soc.* **2007**, *129*, 4643–4654. [[CrossRef](#)] [[PubMed](#)]
41. Zijlstra, N.; Blum, C.; Segers-Nolten, I.M.; Claessens, M.M.; Subramaniam, V. Molecular Composition of Sub-Stoichiometrically Labeled α -Synuclein Oligomers Determined by Single-Molecule Photobleaching. *Angew. Chem. Int. Ed.* **2012**, *124*, 8951–8954. [[CrossRef](#)]
42. Buckle, T.; van der Wal, S.; van Willigen, D.M.; Aalderink, G.; KleinJan, G.H.; van Leeuwen, F.W. Fluorescence Background Quenching as a Means to Increase Signal to Background Ratio—a Proof of Concept During Nerve Imaging. *Theranostics* **2020**, *10*, 9890. [[CrossRef](#)]
43. Kozubenko, E.; Zykina, P.; Krasnoshchekova, E.; Tkachenko, L.; Fedoseeva, K.; Kharazova, A. Method of Reduction Background Fluorescence in Human Fetal Brain Tissue and Quantitative Estimate of the Effect of Photobleaching. *Bull. Exp. Biol. Med.* **2021**, *171*, 100–104. [[CrossRef](#)]
44. Li, X.; Cai, Z.; Jiang, L.-P.; He, Z.; Zhu, J.-J. Metal–Ligand Coordination Nanomaterials for Biomedical Imaging. *Bioconjugate Chem.* **2019**, *31*, 332–339. [[CrossRef](#)] [[PubMed](#)]
45. Tao, P.; Liu, S.J.; Wong, W.Y. Phosphorescent Manganese (ii) Complexes and Their Emerging Applications. *Adv. Opt. Mater.* **2020**, *8*, 2000985. [[CrossRef](#)]
46. Tao, P.; Li, W.L.; Zhang, J.; Guo, S.; Zhao, Q.; Wang, H.; Wei, B.; Liu, S.J.; Zhou, X.H.; Yu, Q. Facile Synthesis of Highly Efficient Lepidine-Based Phosphorescent Iridium (iii) Complexes for Yellow and White Organic Light-Emitting Diodes. *Adv. Funct. Mater.* **2016**, *26*, 881–894. [[CrossRef](#)]
47. Tao, P.; Miao, Y.; Wang, H.; Xu, B.; Zhao, Q. High-Performance Organic Electroluminescence: Design from Organic Light-Emitting Materials to Devices. *Chem. Rec.* **2019**, *19*, 1531–1561. [[CrossRef](#)] [[PubMed](#)]
48. He, Y.; Li, W.; Fu, G.; Wang, B.; Miao, T.; Tan, M.; Feng, W.; Lü, X.; He, H. Efficient and Exclusively NIR-Emitting ($\lambda_{em} = 780$ nm) [ir(C^oN)2(O^oO)]-Heteroleptic Complexes with β -Diketonate-or Pyrazolonate-Typed O^oO-Chelate Ancillary. *J. Lumin.* **2020**, *220*, 116983. [[CrossRef](#)]

49. Penconi, M.; Cazzaniga, M.; Kesarkar, S.; Mussini, P.R.; Ceresoli, D.; Bossi, A. Upper Limit to the Ultimate Achievable Emission Wavelength in NIR Emitting Cyclometalated Iridium Complexes. *Photoch. Photobiol. Sci.* **2017**, *16*, 1220–1229. [[CrossRef](#)]
50. Ikawa, S.; Yagi, S.; Maeda, T.; Nakazumi, H.; Fujiwara, H.; Sakurai, Y. Photoluminescence Color Tuning of Phosphorescent Bis-cyclometalated Iridium (iii) Complexes by Ancillary Ligand Replacement. *Dye. Pigment.* **2012**, *95*, 695–705. [[CrossRef](#)]
51. Demchenko, A.P.; Tomin, V.I.; Chou, P.-T. Breaking the Kasha Rule for More Efficient Photochemistry. *Chem. Rev.* **2017**, *117*, 13353–13381. [[CrossRef](#)] [[PubMed](#)]